Science Arts & Métiers (SAM)
is an open access repository that collects the work of Arts et Métiers Institute of Technology researchers and makes it freely available over the web where possible.

This is an author-deposited version published in: https://sam.ensam.eu
Handle ID: .http://hdl.handle.net/10985/17175

To cite this version :

Jean-Louis OSA, José Antonio SANCHEZ, Naiara ORTEGA, Jean-Luc CHARLES, Ivan IORDANOFF - Discrete-element modelling of the grinding contact length combining the wheel-body structure and the surface-topography models - International Journal of Machine Tools and Manufacture - Vol. 110, p.43-54 - 2016

Any correspondence concerning this service should be sent to the repository Administrator : scienceouverte@ensam.eu

Discrete-element modelling of the grinding contact length combining the wheel-body structure and the surface-topography models

J.L. Osa [a,*], J.A. Sánchez [a], N. Ortega [a], I. Iordanoff [b], J.L. Charles [b]

[a] Mechanical Engineering Department, University of the Basque Country UPV/EHU, Spain
[b] Arts et Métiers ParisTech, I2M-DuMAS, UMR 5295 CNRS F-33405, Talence, France

Keywords:
Grinding contact length
Discrete element method
Topography
Dressing

A B S T R A C T

Phenomena governing the grinding process are largely related to the nature and evolution of contact between grinding wheel and ground component. The definition of the contact area plays an essential role in the simulation of grinding temperatures, forces or wear. This paper presents a numerical model that simulates the contact between grinding wheel and workpiece in surface grinding. The model reproduces the granular structure of the grinding wheel by means of the discrete element method. The surface topography is applied on the model surface taking into account the dressing mechanisms and movements of a single-point dresser. The individual contacts between abrasive grits and workpiece are studied regarding the uncut chip thickness, assuming viscoplastic material behaviour. Simulation results are evaluated with experimental measurements of the contact length. The results remark the importance of surface topography and dressing conditions on the contact area, as well as wheel deflection.

1. Introduction

Technological progress must be based on a deeper scientific knowledge of the process. In this context, research work focused on the modelling and simulation of the grinding process is currently very active. The analysis of the contact between the grinding wheel and the workpiece started in the early 1970s, faced by empirical and semi-analytical approaches. The main authorities in grinding remark the need to consider the contact region in the grinding operation [1,2]. Aspects such as material removal and heat generation take place in the contact region. The granular structure of the grinding wheel and the complex surface topography make difficult to model the operation.

The ideal contact model would be the one that reproduces the structure and stiffness of the wheel, combined with an accurate topography description. This work presents a numerical model of the grinding wheel structure by means of the discrete element method (DEM). Surface topography is applied according to the dressing mechanisms and kinematics of the single-point dresser. The model is used to simulate the contact in surface grinding. The penetration is the reference to estimate the cutting force on each grit. The workpiece material behaviour is assumed viscoplastic, and the effect of the centrifugal force is also taken into account. The aim is to define numerically the contact area and wheel deformation with a complete model that provides a general overview of the grinding operation.

2. Literature review

The literature review collects the main contributions on grinding wheel structure models, surface topography models and contact length models.

2.1. Wheel structure models

The performance of a grinding wheel depends significantly on its structure and morphology. So far, models with noticeable simplifications have been proposed, as [3], which describe wheel elasticity with uniformly distributed spherical grains bonded by elastic springs. Their regular configuration does not match the real random distribution of grains and bonds, creating anisotropic bodies.

Numerical tools like the finite element method (FEM) simulate the mechanical behaviour of a heterogeneous body in an extensive domain. Its main drawback is that it would be very difficult to mesh properly the porous structure of the wheel. In addition, the adjustment of the constitutive relationships of the material and contact conditions would be demanding. The use of multi-scale modelling would decrease the size of the model [4]. To the best of the knowledge of the authors, no finite element model of the wheel structure has been published at the time of sending this

* Corresponding author.
E-mail address: j.osa@ehu.eus (J.L. Osa).

http://dx.doi.org/10.1016/j.ijmachtools.2016.07.004
0890-6955/

Nomenclature

A_d	area of intersection of the diamond and the grain (mm^2)
a, a_e	set and effective depth of cut (μm)
a_d	dressing depth of cut (μm)
b_d, b_s, b_w	width of the dresser, grinding wheel and workpiece (mm)
c	dumping coefficient
d_b	average grit dimension removed by bond fracture (μm)
d_{DE}, d_g	average discrete element and grain diameter (mm)
d_s	grinding wheel diameter (mm)
E_s, E_μ	grinding wheel and beam Young modulus (GPa)
$F_n'^*$, $F_t'^*$	specific normal and tangential force (N/mm)
$\mathbf{f}_c$, $\mathbf{f}_d$	contact and dumping force on a single-grit (N)
$\mathbf{f}_n$, $\mathbf{f}_t$	normal and tangential force on a single-grit (N)
f_{ce}	centrifugal force on a single-grit (N)
f_d	dressing feed (mm/rev)
G^*_{dyn}, G_o	dynamic and theoretical grain density (grains/mm^2)
h_{cu}	uncut chip thickness (μm)
h_f	grit fracture amplitude (μm)
h_s, h_w	grinding wheel and workpiece height on the DEM model (mm)
k^*_m	machine-wheel-workpiece stiffness (N/μm)
l^*_c	contact length (mm)
l_g	geometrical contact length (mm)
L^*	average distance between surface grits (mm)
M	mesh size
M_{iw}	equivalent mass of i element and w workpiece (kg)
N_{DE}	number of discrete elements
N^*_p	number of peaks in the APS signal
N_c	number of discrete elements in contact with the workpiece
N_s	rotation speed of the grinding wheel (rpm)
r	discrete element diameter reduction factor
r_μ	diameter ratio of the beams
r_p	distance between the peak and the discrete element centre (μm)
S	structure number
s	thickness of the mica sheet (μm)
s_n	random number between 0 and 1
t^*_c	contact time (s)
T	temperature (K)
u_d	dressing overlap
v_g	volume of an abrasive grit (mm^3)
V_{DE}	volume of the model domain (mm^3)
V_g	volume fraction of abrasive in the grinding wheel
v_s	cutting speed (m/s)
v_w	work speed (m/s)
$\mathbf{v}_i$, $\mathbf{v}_w$	speed of a discrete element and the workpiece (m/s)
x, y, z	position coordinates (m)
y_p	grit peak depth (μm)
δ_i	penetration of an individual grit on the workpiece (μm)
ε_p, $\dot{\varepsilon}_p$, $\dot{\varepsilon}_o$	plastic strain, plastic strain rate and reference strain rate
μ^*	force ratio
μ_g	grit diameter variation range (mm)
ν_s, ν_μ	Poisson ratio of the grinding wheel and beams
θ	semi-angle of the segment of the grinding wheel DEM model
ρ^*_d	single-point dresser radius (mm)
ρ^*_s	cutting edge sharpness or peak radius (μm)
σ_y	effective yield stress (MPa)

paper.

Li et al. [5,6] propose the first DEM model of the grinding wheel. The model studies the stiffness and resistance of the grinding wheel, the force chain in the bonding material and predicts the surface roughness of the workpiece as a kinematic model. Octahedron discrete elements (DE) substitute SiC abrasive grains. The model is created shaking uniformly distributed elements in position and orientation, like [7,8]. In order to reproduce bonding bridges geometrically and the binder volume fraction, several elastic beams play the role of a single bonding bridge, creating a complex redundant network. In this way, there are several binder spherical DE between the octahedron abrasive DE. Regarding the elements that connects, there are abrasive–binder beams and binder–binder beams. Beam radius is set arbitrarily regarding a fraction of element diameter plus a normal dispersion component. The calibration of beam properties is made by numerical and experimental compression tests, matching the fracture of beams and the noise during tests. In this way, a beam is created if the distance between two intermediate DEs is below a threshold value. However, the resistance under compression is highly dependent on strain rate, which enlarges remarkably the resistance of the conglomerate abrasive–binder at high cutting speeds. The stiffness (or elasticity) is adjusted regarding the load–time slopes in the experimental compression tests. Time is representative of the resistance but not of the stiffness, which is related to the deformation. The model is used to analyse the force chains in the redundant bonding network. The results remark the role of the stresses in tangential direction.

The kinematic model simulates the workpiece roughness, but disregards the effect of dressing. That is the reason for the differences between measurements and numerical surfaces. The octahedron DEs form directly the wheel surface, while the geometry of inner DEs do not play a remarkable role in the structure. The cutting force that acts on each grain is estimated analysing the peaks of experimental force measurements. In this way, the relative position of the surface grit regarding the workpiece (or chip thickness) is neglected, as well as the effect of overlapped peaks. The workpiece is modelled by a rectangular prism composed of DEs. The relationship between workpiece elements is not explained. The authors claim that the model reproduces the material ploughing during grinding, but they do not clarify if the material is removed.

2.2. Surface topography models

Doman et al. [9] review the main topography models presented in the literature. 1D models characterise the surface topography by a single parameter as the grain density, while 2D and 3D models complete the geometrical description of the wheel surface.

The surface topography created by dressing has a direct impact on the performance. Grain and bond fracture are the main dressing mechanisms [2]. The single-point dresser emulates turning movements, levelling out the surface and creating a subtle helix pattern perceptible on the ground surface [7]. Dressing conditions modify the aggressiveness of dressing mechanisms, creating an open softer or a close stiffer wheel surface.

Chen and Rowe [7] create a numerical surface that includes the effect of dressing, using a continuous sinusoidal random function

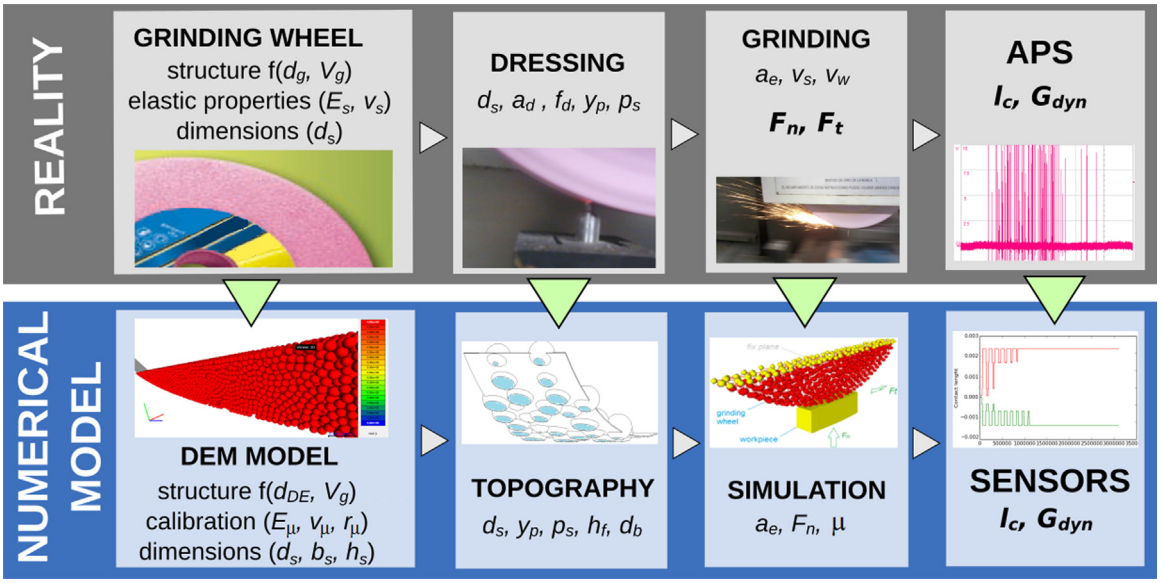

Fig. 1. Flow-chart of the grinding process and analogy of the numerical simulation of grinding.

cuts the grit that interferes. This function y_p has two components: the uniform helix of the diamond $(f(x))$ and a random component that reflects the fragile fracture of grits (Eq. (1)). h_f is the amplitude of the fracture term, ω the random frequency and α the random initial angle. The amplitude h_f of the fragile fracture component y_f is proportional to diamond–grain intersection area A_d and the dressing overlap ratio u_d, and inversely proportional to the dressing feed f_d (Eq. (2)). The effect of the inclination of the diamond tip is disregarded:

$$y_p = y_d + y_f = f(x) + h_f[\sin(\omega x + \alpha) + 1] \tag{1}$$

$$h_f = \frac{A_d \cdot u_d}{4 f_d} \tag{2}$$

Chen and Rowe [7] take into account the bond breakage, regarding the dressing force and the remaining grain size. However, this procedure is not related to the topography. Malkin and Cook [10] deduce the fraction of grains removed by bond fracture, analysing the size distribution of abrasive particles collected during dressing. Eq. (3) relates the surface grain density G_{dyn} and the theoretical grain density G_o regarding the average dressing particle dimension removed by bond fracture d_b. G_o is estimated assuming that a plane cuts the body of the wheel with Eq. (4), where V_g is volumetric abrasive fraction and d_g the average grain diameter. d_b is related to the fraction of abrasive in weight removed by bond fracture and it is defined measuring G_{dyn}:

$$\frac{G_{dyn}}{G_o} = \frac{d_g - d_b}{d_g} \tag{3}$$

$$G_o = \frac{6V_g}{\pi d_g^2} \tag{4}$$

Grain protrusion height has been treated as Gaussian, Weibull and random variable. Simple shapes are chosen to describe asperity geometry. Cutting edges are assumed spherical, conical or frustum, pyramidal and ellipsoidal in shape. Peak geometry reflects the sharpness, which is defined by the cutting edge radius ρ_s (sphere) and slope (cone, frustum, and pyramid). Both are measured analysing 2D profiles of wheel surfaces.

Topography models are rigid, except [7,11], that use springs on surface elements. Thus, they model the surface stiffness, but not the actual body stiffness.

2.3. Contact models

The apparent contact area between wheel and workpiece in surface grinding is determined by the width of pass b_s and the contact length l_c. As b_s is constant, the contact area is characterised by l_c. Supposing that wheel and workpiece are smooth and rigid, the geometrical contact length l_g is defined with Eq. (5) [2], where d_s is the wheel diameter and a_e the depth of cut:

$$l_g = \sqrt{d_s \cdot a_e} \tag{5}$$

However, experimental measurements show that l_c is 1.5–3 times larger than l_g [2]. The problem of estimation of l_c has been tackled from empirical [12,13] and semi-analytical approaches based on Hertz mechanics [14–18] in macro- and micro-scale assuming elastic contact. Lindsay [19] develops a spring model that disregards the depth of cut.

Some characteristics are shared on these models: the topography [14,17,18], the depth of cut [12,14–18], the normal force [14–19] and the elasticity of the grinding wheel and workpiece [14–19]. Only [18] assumes elastoplastic contact, and none considers the effect of the strain-rate, temperature nor cutting. Factors not taken into account are packed into empirical coefficients in all models.

3. Contact length DEM model

The review highlights the importance of surface topography and elasticity of wheel and workpiece in the contact analysis of grinding. But the actual grit–workpiece interaction has been largely disregarded, assuming elastic contact and neglecting the tangential force. A complete contact model combines the stiffness of the bodies, the surface topography and the individual interaction between asperities.

This section describes the construction of the DEM model of the grinding wheel, as well as grit–workpiece contact detection and contact law. The contact DEM model is developed with the GranOO C++ library created at the I2M, ENSAM of Bordeaux. Grinding wheel morphology and structure can be adequately reproduced by DEM, reflecting the randomness of grain size and

position, as well as the elasticity of the wheel. The proposed DEM model represents abrasive grits by spherical discrete elements, while cohesion between grits is brought by elastic beams. A single rectangular discrete element models the workpiece.

The model follows and improves the framework for a general 3D topography model defined by Doman [9], providing elasticity to wheel body. Fig. 1 presents the flow-chart of the grinding process and the numerical contact model in parallel. First, an undressed grinding wheel DEM model is created according to wheel designation and dimensions. Elastic properties are applied through calibration. Then, the dressing generates the surface topography. Contact conditions between individual grits and the workpiece are defined by the contact law.

3.1. Grinding wheel DEM model

The starting point of the DEM model is the grinding wheel designation and dimensions. Grinding wheels are defined according to abrasive material, grain size, hardness grade, structure and bond type. The input parameters to build the DEM model are the average grain diameter d_g, structure and hardness grade.

Grinding wheels are formed of a mix of three or four adjacent grain sizes to control grain density and hardness of the wheel. Grit size is defined by sieve number M and the average grain diameter d_g can be estimated with Eq. (6) [20]. Koshy et al. [8] considers that the grain size follows the normal distribution, hypothesis followed by later authors. However, the grain size distribution seems closer to a uniform distribution in [10], which has been chosen for the DEM model. Eq. (7) defines the range μ_g, being ${d_g}^1$ and ${d_g}^2$ the biggest and smallest grain diameter of the mix regarding meshes used. Eq. (8) estimates the volumetric fraction of abrasive V_g according to the structure number S [20]:

$$d_g = \frac{15.2}{M} \tag{6}$$

$$\mu_g = \frac{d_g^1 - d_g^2}{2} \tag{7}$$

$$V_g = 2(32 - S) \tag{8}$$

The chosen procedure to construct the DEM model is known as numerical sintering [21], which ensures randomness, homogeneity and isotropy. To reduce the size of the model and the computational cost, just a thin slice of the wheel–workpiece set is modelled (Fig. 2). Contact stresses and deformations are concentrated in the contact area. So the model is cut at the height h_s, without altering the contact conditions. h_s is defined by FEM, as the height above which the stress is less than a hundredth of the maximum stress (Fig. 3).

Both, the abrasive volumetric fraction V_g and the average grain

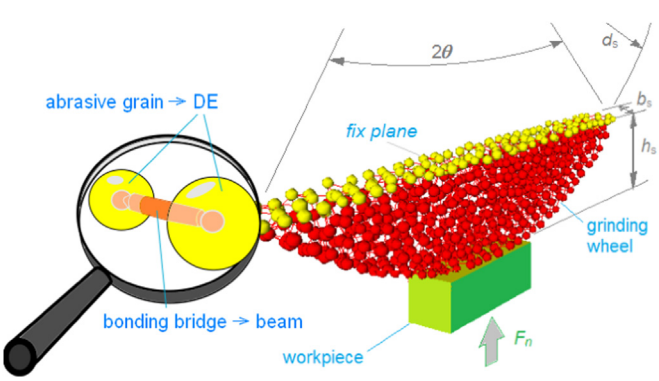

Fig. 2. Contact DEM model (out of scale).

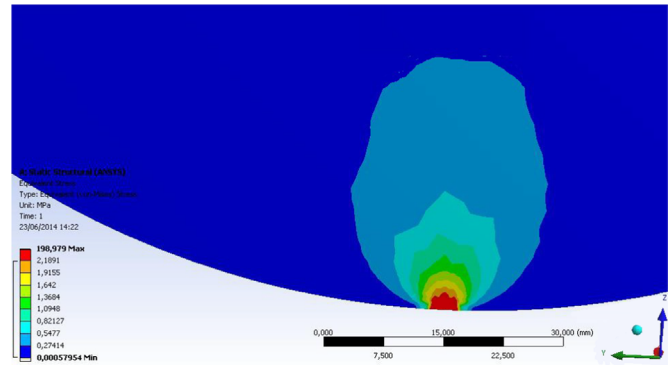

Fig. 3. Stress distribution analysis in the contact zone for the definition of the model height h_s.

diameter d_g, must be adjusted at the same time. First, the number of DE required N_{DE} is estimated with Eq. (9) regarding the volume of the model domain V_{DE}, V_g and v_g grit volume (Eq. (10)), where d_s, b_s and h_s are the wheel diameter, width and height, respectively, and θ is the semi-angle of the arc of the DEM model. The average DE diameter d_{DE} obtained in the DEM model is bigger than the desired d_g, so the diameter of all DE is reduced by the reduction factor r (Eq. (11)). In this way, the DEM model matches V_g and d_g at the same time:

$$N_{DE} = V_{DE} V_g \frac{1}{v_g} = \left[\frac{d_s^2 b_s}{4}\left(\frac{\pi\theta}{360} - \frac{\sin\theta}{2}\right)\right] V_g \left(\frac{6}{\pi d_g^3}\right) \tag{9}$$

$$\theta = 2\arccos\left(1 - \frac{h_s}{d_s}\right) \tag{10}$$

$$r = d_g / d_{DE} \tag{11}$$

3.2. Connecting beams and calibration of mechanical properties

Bernoulli cylindrical beams play the role of bonding bridges, providing stiffness to the DEM model (Fig. 2). Elastic beams are defined by two geometrical parameters (diameter and length L_μ, Fig. 4a) and two mechanical properties (Young's modulus E_μ and Poisson's ratio ν_μ). The diameter of the beam is given by a fraction r_μ of the average diameter of both the DE that connects, so it is straightforwardly defined by r_μ. L_μ is defined by the distance between the centres of the elements that connect the beam. Beam length and orientation variations are updated every iteration. The position of DE centres regarding the initial position sets the interaction forces between grains: axial force, torque and bending moment (Fig. 4b). The formulation of beams is described in [21]. Beams are massless since mass properties are assigned only to DE. Unlike Li et al. [5,6], the volume fraction of binder does not match necessarily the beams volume, because their role is to provide stiffness to the model, not to represent realistically the geometry of bonding bridges.

The hardness grade letter indicates the strength that the bond holds a grit, but it is widely accepted to use wheel's Young's modulus E_s to determine wheel hardness [20]. E_s is measured by sonic testing. A light mechanical impulse incites an initial deformation, which produces a transient mechanical vibration. An analysis in the time domain of the vibration leads the natural frequency of the dominant mode. The frequency of this vibration depends on the mass, the shape and the stiffness of the wheel, and it is used to determine E_s and Poisson's ratio ν_s. Advantages of the sonic test are that it is a non-destructive test and simple to

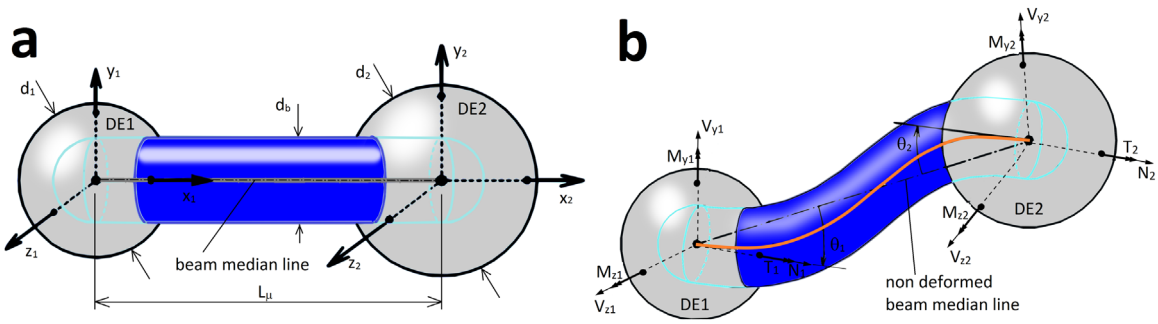

Fig. 4. Elastic beam (a) relaxed and (b) loaded [21,22].

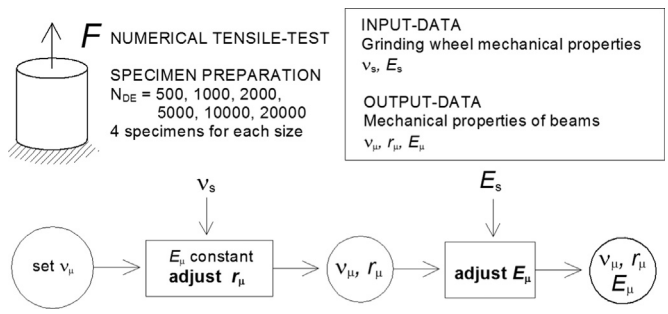

Fig. 5. Flow chart of calibration procedure of the micro-scale properties of the beams [21].

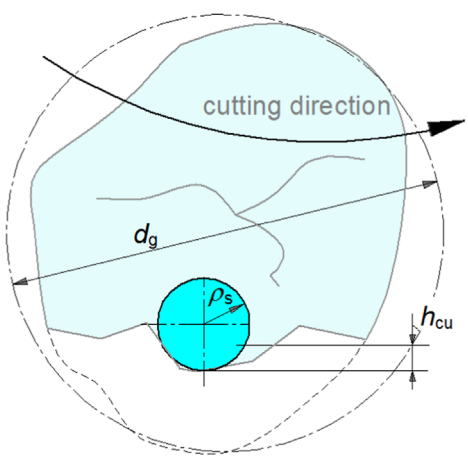

Fig. 6. Grit fractured during dressing and definition of the cutting edge sharpness radius ρ_s (adapted from [2]).

perform.

Unlike FEM, continuous mechanical behaviour laws cannot be directly introduced into DEM formulation. Material properties, as E_s and ν_s, are emergent properties at the macroscopic scale in the DEM model. The micro-scale mechanical properties are calibrated carrying out several tensile numerical tests on cylindrical specimens, following the procedure set by André et al. [21]. There are three micro-scale parameters to calibrate (ν_μ, r_μ, and E_μ) regarding the macro-scale properties (E_s and ν_s). Six model sizes are used in the calibration (500, 1000, 2000, 5000, 10 000 and 20 000 DE) and four models per size. The reason is that using the same input parameters in the DEM model construction, the DEM models are different due to the randomness of the creation procedure. So the result of each model size is the average of four simulations. Numerical tensile tests measure the axial and transversal strain of the specimens, which allows the definition of the macro-scale properties. Analysing the results graphically, the micro-scale properties

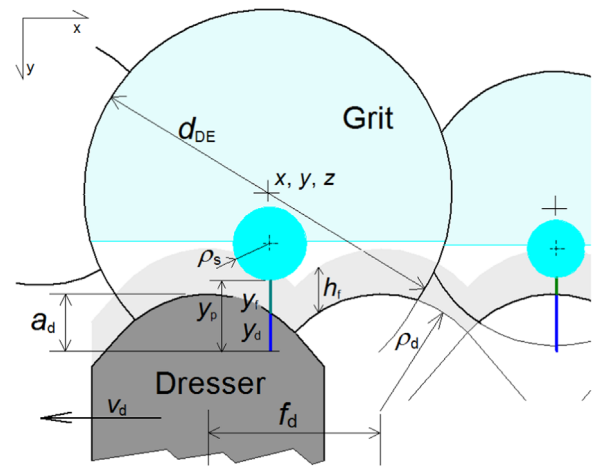

Fig. 7. Implementation of dressing on the DEM model surface; the peak is located at the radial depth y_p regarding the wheel diameter d_s and aligned with the DE centre; y_p is the sum of the ductile cutting of the dresser y_d and abrasive fracture term y_f (adapted from [7]).

are fitted regarding the macro-scale properties.

Fig. 5 shows the flow chart of the calibration of beam properties. The micro-scale ν_μ, r_μ and E_μ parameters affect in a different way to the macro-scale properties. For any specimen size, ν_μ has scarce influence on macro-scale properties. With that in mind, the calibration is performed in two steps. First, ν_μ is set as ν_s, sparing a variable. Maintaining E_μ fixed, the influence of r_μ on ν_s is studied. Once r_μ is set, the second step is to analyse the influence of E_μ on E_s. In that way, the three micro-scale variables are set and these are independent to the model size, DE size or abrasive fraction. The mechanical properties are applied after creating the DEM model and before run the simulation.

3.3. Topography of grinding wheel surface

The topography is applied on the DEM model in four steps: (1) levelling out the surface, (2) remove the fraction of grains released by bond fracture, (3) set the peak radial depth and (4) the average cutting edge radius (Fig. 6).

The diamond breaks up the abrasive grits that intercepts in a brittle manner. This effect is modelled cutting off the DEM model surface at the grinding wheel diameter d_s. Therefore, DEM model is constructed with a diameter slightly larger than d_s, avoiding the effect of grain pile up at the surface at the same time. Then, the fraction of grains pulled out by bond fracture is removed regarding Malkin's model [10]. The average dressing particle dimension removed by bond fracture d_b is estimated with Eq. (3) regarding experimental grain density measurements G_{dyn}. In this way, the

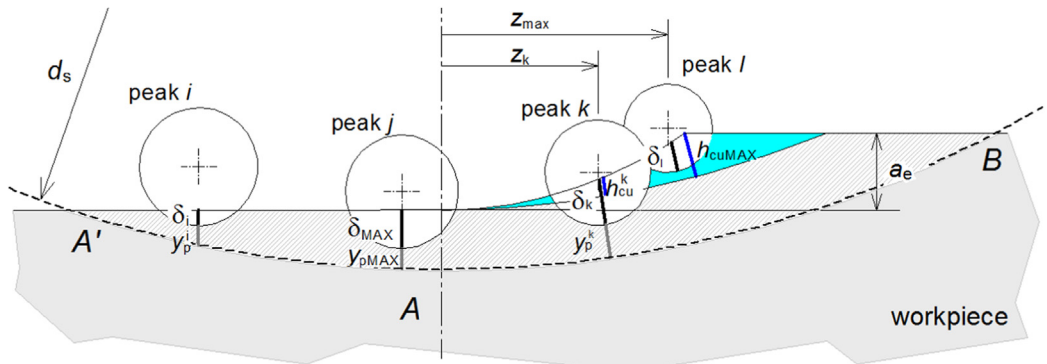

Fig. 8. Contact detection on A'–A and A–B segments, the circles represent grain peaks. Peak depth $y_p{}^i$ is defined regarding the wheel diameter d_s and δ_i is the penetration regarding the workpiece surface. The corresponding uncut chip thickness h^i_{cu} is added in the A–B segment.

intercepted elements by the cylindrical surface d_s with a diameter smaller than d_b are removed from the model surface.

Now the DEM model surface is ready to be treated. First, the peak position in radial depth y_p is defined for each surface DE. Regarding [23], each surface grit has a single useful cutting edge or peak (Fig. 6). In the DEM model, the peak radial depth y_p is defined applying Chen's sinusoidal function on DE centres as a discrete function (Fig. 7). Chen's topography model is chosen, even though the simple definition of the fracture term, which is dominant, because the combination of the dresser helix and fracture term creates an acceptable topography to model the contact. Eq. (12) reminds Eq. (1), combining the effect of helix ductile cut y_d and abrasive fracture y_f. The intersection of the vertical line that crosses the DE centre and circumference function with a moving centre placed in multiple of the dressing feed f_d defines y_d (Eq. (13)). In Eq. (13), ρ_d is the radius of the single-point dresser, x_c and y_c are the instantaneous dresser position, x is the axial position of the peak or DE centre and a_d is the dressing depth of cut. x_c is a discrete number proportional to the feed f_d and its value is defined rounding the nearest value to DE centre x. And Eq. (14) defines y_f as a random fraction s_n of the fracture term amplitude h_f, defined by Chen in Eq. (2). In this way, the grain peak resembles the most protuberant cutting edge (Fig. 6) and the grain density arises according to radial depth y_p:

$$y_p(x) = y_d(x) + y_f \tag{12}$$

$$y_d(x) = \sqrt{\rho_d^2 - (x - x_c)^2 - y_c} \text{ where } x_c = \mathbb{Z}\left(\frac{x}{f_d}\right) \text{ and } y_c = a_d - \rho_d \tag{13}$$

$$y_f = h_f \cdot s_n \tag{14}$$

Regarding peak geometry, the cutting edge sharpness is modelled with the sharpness radius ρ_s. It offers a variable slope and bearing surface through depth, as well as it can indicate the wear condition. The cutting edge radius ρ_s is measured analysing two 2D profiles of grain peaks on the cutting direction [24]. As grit–workpiece contact is superficial, ρ_s is defined as the circle inscribed within a few microns depth.

3.4. Boundary conditions

In order to simulate the contact, grinding forces are applied on the workpiece, whereas the cutting plane of the DEM model is fixed and the centrifugal force is applied on each element (Fig. 2). The simulation starts from a non-contact almost-touching position ($< 10^{-16}$ m) to optimise the computation time. First, the normal force is applied first as a ramp to assure the dynamic stability, becoming constant when the nominal normal force is reached. The experimentally measured normal and tangential forces are applied on the workpiece. The positions of surface elements and the workpiece are compared on each iteration according to the depth of cut a_e, applying a reaction force if an interpenetration is detected. During simulation, the actual maximum penetration, resultant contact force and contact length are monitored. The simulation finishes when the damped system gets balanced, that is, the applied force on the workpiece equals the resultant of grit reactions.

3.4.1. Contact detection

Studying Fig. 8, the geometric contact length l_g is defined by the arc A–B and the starting point A coincides with the bottom quadrant of the wheel. Due to wheel deformation, the contact area enlarges to A' point. The model supposes that, on the A'–A quadrant, the grains plough plastically the workpiece surface and, on the A–B quadrant, the analytical uncut chip thickness h_{cu} is added to the plastic deformation reached in A'–A. On both sides, the

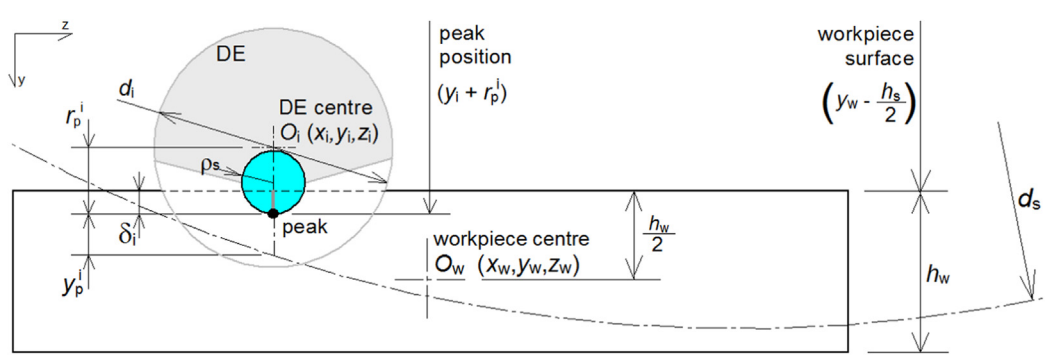

Fig. 9. Contact detection at the A'–A segment between a surface DE and workpiece: peak position is compared with workpiece position to determine the penetration δ_i.

penetration of the grits δ_i coincides with the actual h_{cu}, which is used to estimate the force on each grit. The effect of the tracks left by previous grits is disregarded, as well as the material pile up.

The contact detection algorithm differs on both sides. Regarding Fig. 8, on the *A'–A* segment a contact is detected if the interpenetration grit–workpiece δ_i is positive when comparing their positions at each iteration (Fig. 9). Eq. (15) introduces the contact detection expression. The penetration δ_i is the difference between the grit peak $(y_i + r_p^i)$ and workpiece surface $(y_w - h_w/2)$ positions. ${r_p}^i$ is the distance between peak and DE centre, (x_i, y_i, z_i) and (x_w, y_w, z_w) are DE centre and workpiece position coordinates, respectively, and h_w is the workpiece height. The distance ${r_p}^i$ is defined before simulation, regarding the DE initial position, d_s the wheel diameter and ${y_p}^i$ the peak radial depth.

$$\delta_i = (y_i + r_p^i) - \left(y_w - \frac{h_w}{2}\right) \tag{15}$$

On the *A–B* segment, the elements that take part are the ones placed on a distance of the depth of cut a_e from the workpiece DE surface. Due to the real curvature of the contact zone is unknown, the indentation on the *A–B* segment takes the peak depth y_p as floating reference (Eq. (16)). Thus, the penetration δ_k is the sum of the maximum indentation on the *A'–A* side δ_{MAX} plus the correspondent uncut chip thickness ${h_{cu}}^k$, taking into account peak height differences y_p (Fig. 8). A positive δ_k within a_e distance from the workpiece surface confirms the contact. Supposing that h_{cu} varies lineally through the contact arc, its value is estimated regarding the maximum uncut chip thickness h_{cuMAX} and the element longitudinal relative position z_k regarding the maximum horizontal contact detected z_{MAX} (Eq. (17)). Eq. (18) estimates h_{cuMAX} [2], where L is the average distance between grits, v_w and v_s are the working and cutting speeds, a_e is the depth of cut and d_s is wheel diameter:

$$\delta_k = \left(\left(\delta_{MAX}^{A'-A} + y_{MAX}^p\right) - y_p^k\right) + h_{cu}^k \tag{16}$$

$$h_{cu}^k = h_{cuMAX} \cdot \frac{z_k}{z_{MAX}} \tag{17}$$

$$h_{cuMAX} = 2L\frac{v_w}{v_s}\sqrt{\frac{a_e}{d_s}} \tag{18}$$

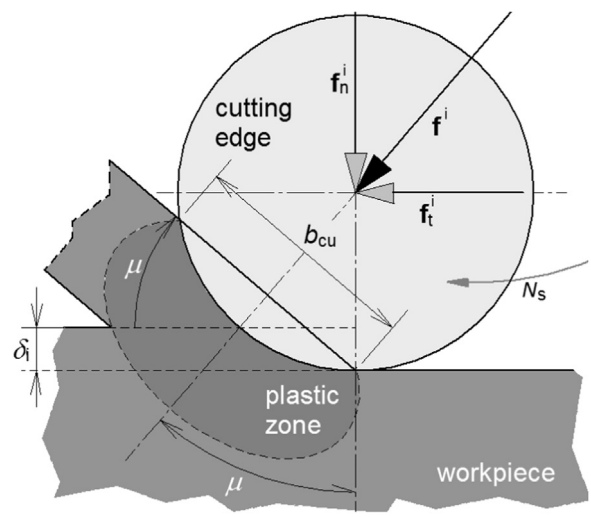

Fig. 10. Analogy of the hardness model of chip formation [1].

Table 1
Test conditions, instruments, experimental results and simulation input data

Grinding wheels			
300x76.2x30 mm		A46I8V	A60K7V
Abrasive volume fraction, V_g (%)		48	50
Average grain diameter, d_g (mm)		0.330	0.253
Young's modulus, E_s (GPa)		32	43
Poisson ratio, ν_s		0.2	0.2
Density (kg/m^3)		1854	2096
Model dimensions, $d_s x b_s x h_s$ (mm)		300x2.24x5.1	300x1.7x5.1
Number of DEs, N_{DE}		11 000	19 100
Dressing conditions			
Coarse (C)	$a_d = 20$ µm	$f_d = 0.8$ mm/rev	$u_d = 1$
Medium (M)	$a_d = 20$ µm	$f_d = 0.4$ mm/rev	$u_d = 2$
Fine (F)	$a_d = 20$ µm	$f_d = 0.2$ mm/rev	$u_d = 4$
Needle type single point dresser		$b_d = 0.8$ mm	$\rho_d = 4.06$ mm
Force measurements			
Dynamometer plate: Kistler 9257B		500 Hz, force range $\pm$1000N	
Four runs per test condition		$a = 10$ - 20 µm	$v_s = 24$ m/s $\quad v_w = 0.5$ m/s
Topography		Confocal microscope	Leica DCM3D
Grain density and contact length			
Applied power source (APS)		Oscilloscope Lecroy waveRunner 104Xi	
12 runs per test condition		Mica sheet thickness 40 µm	

	A46I8V			A60K7V		
	F	M	C	F	M	C
d_b (µm)	233	243	259	178	188	199
h_{cuMAX} ($a = 10$ µm)	0.34	0.39	0.51	0.31	0.34	0.4
h_{cuMAX} ($a = 20$ µm)	0.52	0.58	0.7	0.48	0.48	0.54

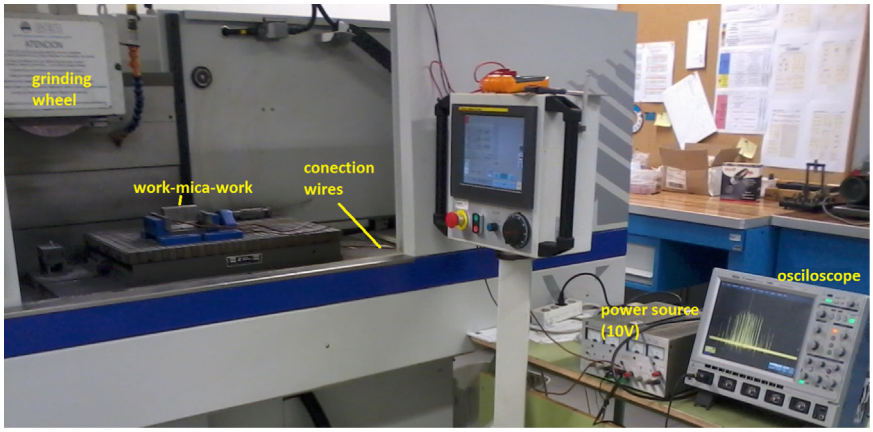

Fig. 11. Experimental set-up of the applied power source method.

3.4.2. Contact law

The contact force is used along with neighbour DE interactions to calculate the speed and position of the elements in the following iteration.

Shaw [1] proposes the analogy of the hardness model to explain the chip formation in grinding. The maximum shear stress slip-lines in grinding resemble the ones produced testing material hardness (Fig. 10). As hardness model, Shaw deduces the reaction as plastic-perfect rigid contact. However, plastic strain and the high strain-rate increase material resistance, while high temperatures weaken the material. The viscoplastic behaviour describes the inelastic behaviour of materials regarding the strain-rate and temperature. The Johnson–Cook (JC) model is used to estimate the effective yield stress σ_y [25]. The penetration δ_i of the grit in the workpiece (or chip thickness h_{cu}) is the main input of the hardness model.

Once detected the contact, the same and opposite normal $\mathbf{f}_n^i$ and tangential $\mathbf{f}_t^i$ contact forces are added to the element and the workpiece $\mathbf{f}_n^i$ and $\mathbf{f}_t^i$ are related by the experimentally measured force ratio μ (Eq. (19)). The normal reaction force on a grit $\mathbf{f}_n^i$ (Eq. (20)) has a contact reaction term $\mathbf{f}_c$ deduced with Shaw's model (Eq. (21)) and a dumping term $\mathbf{f}_d$ (Eq. (22)):

$$\mathbf{f}_t^i = \mu \cdot \mathbf{f}_n^i \tag{19}$$

$$\mathbf{f}_n^i = \mathbf{f}_c + \mathbf{f}_d \tag{20}$$

$$\mathbf{f}_c = 3\sigma_y \pi \left[\rho_s \sin\left(\arccos\left(\frac{\rho_s - \delta_i}{\rho_s} \right) \right) \right]^2 \cdot \sin\left(\arctan\mu \right) \cdot \mathbf{n} \tag{21}$$

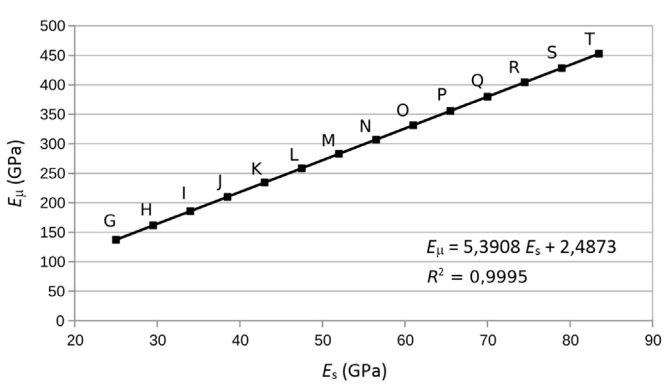

Fig. 12. Correspondence between the wheel grade (G–T), the elastic modulus E_s and the micro-scale beam's elastic modulus E_μ.

Table 2
Micro-scale beam properties.

Grinding wheel	Micro-scale Poisson ratio, ν_μ	Micro-scale diameter ratio, r_μ	Micro-scale modulus, E_μ (GPa)
A46I8V	0.2	0.538	175
A60K7V	0.2	0.538	234

$$\mathbf{f}_d = 2c\sqrt{E_s M_{iw}}\,[(\mathbf{v}_i - \mathbf{v}_w)\cdot\mathbf{n}]\cdot\mathbf{n} \tag{22}$$

$\mathbf{f}_c$ and $\mathbf{f}_d$ are aligned with $\mathbf{n}$, the vertical unit vector. Even DE are spheres of d_g average grain diameter, a sphere of ρ_s radius represents the cutting edge sharpness. The dumping term $\mathbf{f}_d$ is related to the penetration speed. In Eq. (22) c is the dumping coefficient, E_s Young's modulus of the wheel, $M_{iw} = \frac{m_i \cdot m_w}{m_i + m_w}$ the equivalent mass of DE and workpiece couple, and $\mathbf{v}_i$, $\mathbf{v}_w$ the speeds of the element and the workpiece. The dumping coefficient c does not affect on simulation results, but dissipates energy from both bodies. So a high c is chosen to accelerate the convergence.

3.4.3. Centrifugal force

The centrifugal force $\mathbf{f}_{ce}$ is applied on each DE, regarding the mass of the DE m_i, rotation speed of the wheel N_s and distance from wheel centre, which is calculated with y_i and z_i position coordinates. $\mathbf{f}_{ce}$ is applied on the radial direction and Eq. (23) defines the value of the module f_{ce}^i:

$$f_{ce}^i = m_i \cdot \left(\frac{\pi N_s}{30} \right)^2 \sqrt{y_i^2 + z_i^2} \tag{23}$$

4. Validation of the DEM contact model

Several tests and correspondent simulations have been performed in order to validate the contact model. Experimental tests supply the input data for the simulations as well as the aimed contact length. On the one hand, input data is provided by force measurements (forces and depth of cut), topography measurements (sharpness radius and average distance between grits) and the applied power source (APS) (grain density). On the other hand, the APS also measures the contact length, the output of the contact model.

Before running the simulations, the mechanical properties of the beams are calibrated according to wheel grade. To overcome the randomness of the DEM models, four models are created with the same parameters for each grinding wheel type. In the pre-processing, their surface is modified to reproduce the topography and the experimental forces and constraints are applied on the

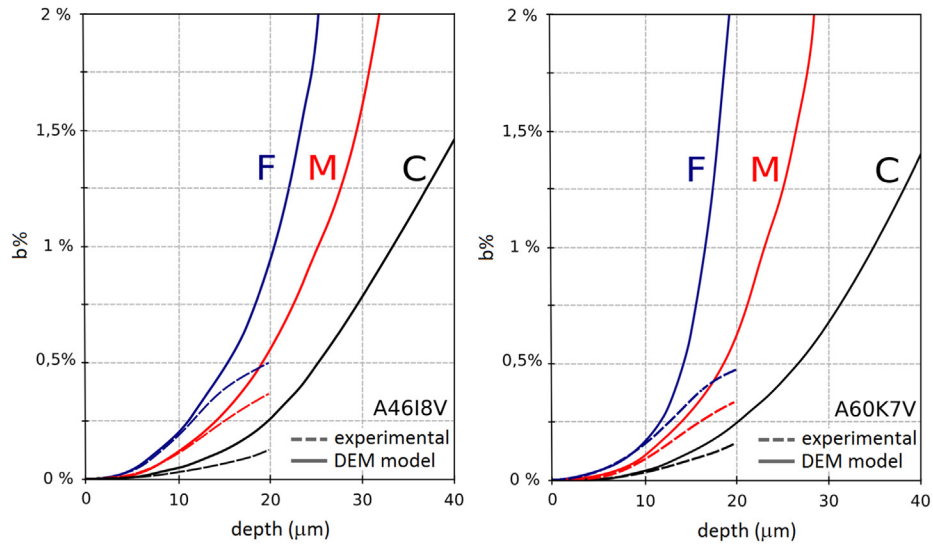

Fig. 13. Experimental and numerical bearing ratio curves of DEM model surfaces regarding grinding wheel (A46I8V, A60K7V) and dressing condition (F, M, and C).

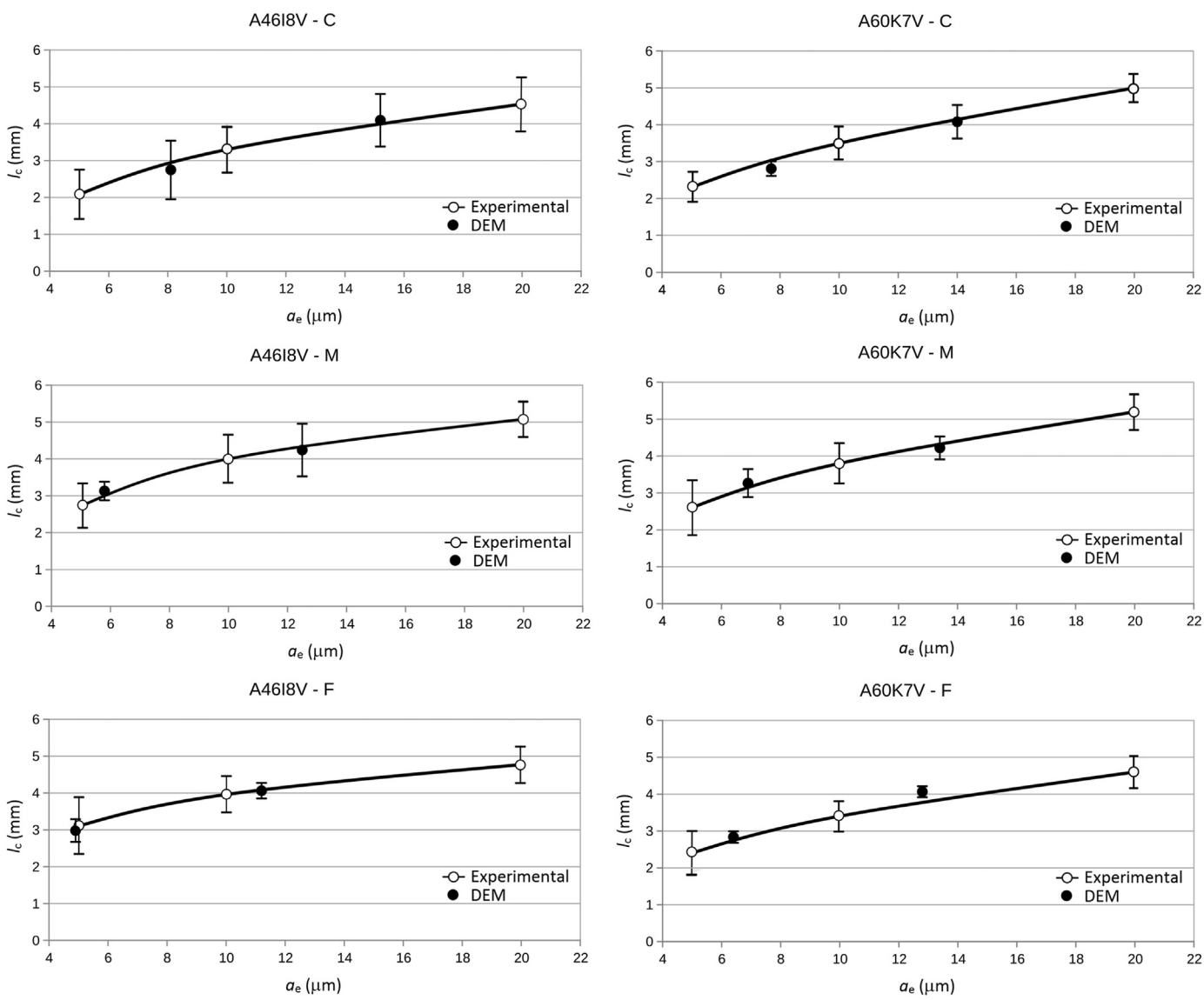

Fig. 14. Contact length experimental measurements and numerical results, according to the grinding wheel type (A46I8V on the left and A60K7V on the right) and dressing condition (C, M, and F).

Table 3
Experimental and numerical results of contact length, maximum penetration and dynamic grain density

A46I8V	Experimental tests					DEM model					
dressing-a	F'_n (N/mm)	μ	l_g (mm)	l_c (mm)	G_{dyn} (grits/mm^2)	l_c (mm)	*Error(%)* l_c	δ_{MAX} (μm)	N_c	G_{dyn} (grits/mm^2)	*Error(%)* G_{dyn}
C-10	4.2	0.49	1.56	2.88	1.28	2.75	-4.6%	6.35	9.8	1.35	5.2%
C-20	10.5	0.49	2.14	4.14	1.58	4.09	-1.1%	7.01	18.2	1.68	6.2%
M-10	9.3	0.55	1.32	2.96	2.05	3.13	5.8%	4.78	18.4	2.22	8.6%
M-20	16.4	0.5	1.94	4.45	2.37	4.24	-4.7%	6.87	23.4	2.1	-11%
F-10	11.2	0.53	1.22	3.08	2.62	2.98	-3.2%	4.28	22.6	2.87	9.5%
F-20	19.3	0.49	1.84	4.12	2.93	4.06	-1.4%	6.01	30.4	2.83	-3.5%
A60K7V	**Experimental tests**					**DEM model**					
dressing-a	F'_n (N/mm)	μ	l_g (mm)	l_c (mm)	G_{dyn} (grits/mm^2)	l_c (mm)	*Error(%)* l_c	δ_{MAX} (μm)	N_c	G_{dyn} (grits/mm^2)	*Error(%)* G_{dyn}
C-10	5.0	0.44	1.52	2.99	1.83	2.81	-6.1%	6.5	11.5	1.86	1.5%
C-20	13.3	0.47	2.05	4.24	2.38	4.08	-3.7%	12.7	20.2	2.26	-5.6%
M-10	6.9	0.45	1.44	3.1	2.17	3.27	5.4	5.6	15.7	2.19	1.1%
M-20	14.4	0.5	2.01	4.43	3	4.22	-4.7%	7.2	25.7	2.77	-7.6%
F-10	7.8	0.49	1.39	2.71	2.83	2.84	4.6%	3.6	19.5	3.13	10%
F-20	15.8	0.49	1.96	3.84	3.23	4.07	5.9%	6.5	28.5	3.19	-1.4%

model. In the processing, the new position of each DE is calculated on each iteration. Finally, the monitored data are analysed and the grinding contact length is estimated as the average of the four simulations per testing condition.

4.1. Test conditions and experimental results

Table 1 compiles the measuring instruments and testing conditions. Two vitrified alumina grinding wheels (A46I8V and A60K7V) have been tested under three dressing conditions (fine (F), medium (M) and coarse (C)) and two set depth of cut a (10–20 μm). All measurements have been performed without coolant in the surface grinder GER SC 60/40.

Experimental grinding forces are directly introduced in the model as input. During simulation the force is the reference value of the solution, as the resultant of individual grit reaction forces converges with the force. The effective depth of cut a_e is estimated regarding the machine–tool–workpiece system stiffness k_m (Eq. (24)) [2]:

$$a_e = a - \frac{F'_n}{k_m} \tag{24}$$

The single-point dresser is a needle like synthetic diamond. It has the advantage that maintains the profile through the working life. Its profile is almost flat of radius ρ_d=4.06 mm, two orders bigger than the dressing depth of cut.

2D profiles have been analysed in the cutting direction to define the sharpness radius of the cutting edge ρ_s. 3D topography measurements allow us to identify the most protuberant peaks for 2D profiles. Just the end of the peak removes material in a shallow manner, so the circle of the edge fits the first 5 μm. Similar ρ_s values have been observed for different dressing conditions. An average ρ_s of 29 μm and 27 μm are observed on A46I8V and A60K7V, respectively, with a standard deviation of 4.6 μm and 3.8 μm. The same profiles have been used to measure the average distance between grits L regarding [23].

Due to its accuracy, the APS method [26] has been chosen to measure the contact length l_c, as well as the dynamic grain density G_{dyn}. The APS follows the principle of an open and close circuit (Fig. 11). The workpiece is divided in two parts isolated by a mica sheet and both are connected to an electric potential source of 10 V. When a grit passes over the protuberance, the circuit switches on and a voltage is measured by the oscilloscope. The study of the tension signal over time leads the estimation of the

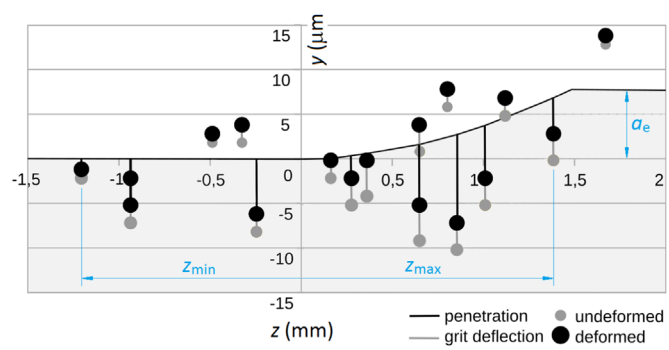

Fig. 15. Example of wheel deformation: position of surface peaks unloaded and loaded (A60K7V, a=10 μm, C dressing).

contact time t_c. Thus l_c is defined with Eq. (25), where v_w is the work speed and s the thickness of the insulation layer. In the same way, G_{dyn} is defined as the amount of tension peaks (or contacts) N_p over the contact area, l_c by protuberance width b (Eq. (26)). Tests are performed under three set depths of cut a=5–10–20 μm, two protuberance widths b=0.15–0.5 mm and 12 runs per test condition:

$$l_c = v_w \cdot t_c + s \tag{25}$$

$$G_{dyn} = \frac{N_p}{l_c \cdot b} \tag{26}$$

4.2. DEM model set-up

Before running the simulation, beam properties are calibrated to match the elasticity of the wheel and surface topography is applied. The calibration has been made for the whole range of wheel grades (G–T). Calibration results are valid for any grit size and structure number. Several cylindrical DEM specimens of different sizes are prepared for the tensile numerical tests. Setting the micro-scale Poisson ratio at $\nu_\mu = 0.2$, a diameter ratio of $r_\mu = 0.538$ is obtained for a macro-scale ν_s of 0.2 [20]. The second step of the calibration leads a regression curve (Fig. 12) that relates the macro- and micro-scale Young modulus $(E_s,\ E_\mu)$ for the whole range of hardness grades. Table 2 introduces the micro-scale parameters obtained in the calibration.

The topography is applied in the pre-processing on each

simulation regarding the procedure described in Section 3.3. Fig. 13 compares the bearing curves measured experimentally (continuous lines) and the ones obtained applying Chen's model in the DEM model (discontinuous lines). Chen's bearing ratio is obtained regarding only the cutting edges on the DEM model surface. The superposition of both coincides up to in 10 µm depth, where the experimental bearing ratios increase rapidly. This is due to the application of Chen's model in a discrete manner only on grit peaks. However, as the penetration of the cutting edges lays within the range of 10 µm, the discrete application of Chen's model is valid to simulate the contact.

The JC model defines the yield criterion regarding the strain rate and temperature (Eq. (27)). The material constants for tool steels have been taken from [25]. In Eq. (27) ε_p is the plastic strain, $\dot{\varepsilon}_p$ is the actual plastic strain rate, $\dot{\varepsilon}_o$ is the reference strain rate and T is the actual temperature of the material. These three parameters vary along the trajectory of a grit in contact with the workpiece (rubbing, ploughing and cutting). They can be estimated by numerical models [27]. In turn, the experimental determination of the shear angle, ε_p, $\dot{\varepsilon}_p$ and temperature regarding the cutting edge penetration requires an extensive single-grit cutting research. In this research, their values are assumed constant through the contact arc. For an average chip thickness of h_{cu}=4 µm, a cutting speed of v_s=24 m/s, a rake angle of $\alpha = -60°$ and a temperature of 950 K, obtaining an effective yield stress σ_y of 810 MPa. These values agree with the ones obtained by [27]. The error that supposes the assumption of constant deformation and temperature parameters is smaller than neglecting the viscoplastic behaviour of the workpiece material:

$$\sigma_y\left(\epsilon_p, \dot{\epsilon}_p, T\right) = \left[1860 + 477\epsilon_p^{0.18}\right]\left[1 + 0.012\ln\frac{\dot{\epsilon}_p}{\dot{\epsilon}_o}\right]\left[1 - \left(\frac{T - 280}{1763 - 280}\right)\right] \tag{27}$$

4.3. Simulation results and discussion

Fig. 14 summarises experimental and numerical contact lengths for each grinding wheel and dressing condition. Table 3 compiles the same results, adding the maximum penetration δ_{MAX} and the grain density G_{dyn}. The experimental-geometrical contact length ratio (l_c/l_g) is between 1.85 and 2.52 for A46I8V wheel and between 1.92 and 2.2 for A60K7V, as described in the literature [2].

The DEM model has grasped the randomness of grinding, so all results are defined by the average and the standard deviation. Fig. 14 shows the standard deviations of the experimental and numerical contact length results. The dispersion of numerical results is generally narrower than the ones observed in the tests.

l_c simulation results are close to the experimental ones (up to 6% error). On both wheels, l_c seems not to increment according to the dressing condition within the tested range. Wheel grade, centrifugal forces and cutting edge sharpness parameters are similar in both wheels, regardless the dressing condition. Then, the compelling parameters are the specific normal force F_n', the depth of cut a_e and the surface grain density G_{dyn}. In turn, G_{dyn} depends on wheel characteristics (average grain diameter d_g and volumetric fraction of abrasive V_g) and dressing conditions (average particle dimension removed by bond fracture d_b, dresser radius ρ_d and overlap ratio u_d). Grain density and peak depth determine the bearing ratio of the surface or the supporting surface through radial depth.

Under fine dressing conditions, grinding forces are higher and, thus, a_e decreases. In turn, the medium dressing (M) obtains larger l_c than the fine (F) one within the range of variables tested. Marinescu [2] asserts that dressing determines the contact stiffness, which is directly related to the bearing ratio. Coarse dressing (C) gets the lowest grain density and maximum penetration δ_{MAX} with the highest a_e. The single-grit force is related exponentially with the penetration, so less grains stand higher loads penetrating deeper. In turn, the higher G_{dyn} and, thus, bearing ratio of the fine dressing reduces the penetration in the workpiece. The medium dressing condition meets the combination of a_e and grain density that obtains the largest contact lengths on both wheels. This confirms the relationship between contact stiffness and bearing ratio, hence dressing.

The DEM model also offers an insight about wheel deformation and contact stiffness. It asserts the grain deflection magnitudes stated in the literature, about 5 µm [1]. The maximum grain deflection is 3.7–9.1 µm for A46I8V and 2.9–6.6 µm for A60K7V. The force intensity on each cutting edge is defined by F_n'–G_{dyn} relationship, but grit deflection depends also on the number of beams and the relative position with adjacent grits. Fig. 15 shows an example of deflection (A46I8V, a=10 µm, C dressing). The contact length is defined as the largest distance between grits in contact, the sum of z_{max} and z_{min}. Some surface grits that do not get in touch with the workpiece are also displaced due to the beam network. The black line represents the workpiece surface and the relative position of the cutting edges (black circles) determines the penetration. The elastic deformation of surface grits contributes to the enlargement of the contact length. The average maximum penetration δ_{MAX} is 6 µm , which agrees the results of [23]. A singular peak of 13 µm appears in the A46K7V with coarse dressing and a = 20 µm, probably due to the concentration of load on a low density area.

The DEM model foresees the grain density too. As the experimental estimation of G_{dyn} with APS, Eq. (26) is used to calculate G_{dyn} replacing the number of peaks N_p by the number of DEs in contact N_c. Numerical G_{dyn} results differ from the measured ones (up to 10%). The differences are not proportional under the same dressing conditions. However, the large dispersion of experimental G_{dyn} measurements (up to 0.4 grits/mm^2) remarks the uncertainties in the APS results.

The model also allows us to analyse interesting aspects, such as the average and maximum force per grit, or the apparent contact pressure. The average force per grit is 1–1.5 N for the A46I8V and 0.7–1.1 N for the A60K7V. These highlights the role of the grain density in the material removal. The maximum force per grit reaches up to 28 N for A46I8V and 4.6 N for A60K7V. These values are interesting to analyse the stresses in the bonding material. Regarding the apparent contact pressure, it is 1.5–4.7 Pa for the A46I8V and 1.8–3.9 Pa for the A60K7V. The apparent pressure hides the ploughing and cutting processes under the apparent contact area, so these values have to be treated carefully.

Wheel grade, centrifugal forces and cutting edge sharpness are not studied in the simulations. Higher wheel grade makes the wheel stiffer. Higher centrifugal forces increase the stiffness of the wheel. Sharper cutting edges lead more efficient material removal, increasing the depth and, thus, the contact length.

5. Conclusions

A numerical methodology has been presented to simulate the contact grinding wheel–workpiece in surface grinding. The 3D structure of the grinding wheel is built by means of DEM. The surface topography is implemented applying Chen's model in a discrete manner. The combination of Shaw's hardness model for single-grit cutting and a viscoplastic behaviour of the workpiece leads the estimation of the contact reaction between a surface element and the workpiece.

DEM has proved to be a valuable tool for the modelling of grinding wheels. Simulation results fit well with the experimental contact length measurements within the 6%. The model captures the influence of the surface topography and it highlights the combined effect of the normal force, depth of cut and grain density. Shaw's indentation analogy of single-grit force has shown its potential for the estimation of grinding forces in a simple way. But the key of its success is on the viscoplastic material assumption, which surprisingly has been disregarded so far in the contact models. Chen's topography combined with Malkin's grain release model reproduce the peak distribution through depth regarding dressing conditions. The combination has shown the sensitivity to capture dressing hints on grinding forces. The DEM model of the grinding wheel has proved the capacity to reproduce the wheel's granular nature and stiffness, leading the modelling of wheel deflection when grinding. Among all, the combination of DEM wheel body and surface topography stands out because of the description of the randomness of the grinding wheel, reflected on the dispersion observed in the results. The versatility of the model formulation allows the further adaptation for other purposes, like the workpiece surface roughness, contact stiffness, grit pull-out, grinding forces, effect of the centrifugal force or thermal analysis including the wheel.

Acknowledgement

The authors gratefully acknowledge the funding support received from the Spanish Ministry of Economy and Competitiveness and the FEDER operation program for funding the project *Optimización de procesos de acabado para componentes críticos de aerorreactores* (DPI2014-56137-C2-1-R). The authors thank for technical and human support provided by IZO-SGI SGIker of UPV/EHU and European funding (ERDF and ESF). The DEM simulation have been carried out thanks to the free software GranOO, distributed at www.granoo.org and thanks to the help of the GranOO team.

References

[1] M.C. Shaw, Principles of Abrasive Processing, Oxford University Press, Oxford, UK, 1996.
[2] I.D. Marinescu, W.B. Rowe, B. Dimitrov, I. Inaski, Tribology of Abrasive Machining Processes, Elsevier, Waltham, USA, 2004.
[3] M. Moser, Microstructures of Ceramics: Structure and Properties of Grinding Tools, Akadémiai Kiadó, Budapest, Hungary, 1980.
[4] P. Kanouté, D. Boso, J. Chaboche, B. Schrefler, Multiscale methods for composites: a review, Arch. Comput. Methods Eng. 16 (1) (2009) 31–75.
[5] H. Li, T. Yu, L. Zhu, W. Wang, Analysis of loads on grinding wheel binder in grinding process: insights from discontinuum-hypothesis-based grinding simulation, Int. J. Adv. Manuf. Technol. 78 (9–12) (2015) 1943–1960.
[6] H. Li, T. Yu, L. Zhu, W. Wang, Modeling and simulation of grinding wheel by discrete element method and experimental validation, Int. J. Adv. Manuf. Technol. (2015) 1–18.
[7] X. Chen, W.B. Rowe, Analysis and simulation of the grinding process. Part I: generation of the grinding wheel surface, Int. J. Mach. Tools Manuf. 36 (8) (1996) 871–882.
[8] P. Koshy, V. Jain, G. Lal, Stochastic simulation approach to modelling diamond wheel topography, Int. J. Mach. Tools Manuf. 37 (6) (1997) 751–761.
[9] D. Doman, A. Warkentin, R. Bauer, A survey of recent grinding wheel topography models, Int. J. Mach. Tools Manuf. 46 (3) (2006) 343–352.
[10] S. Malkin, N.H. Cook, The wear of grinding wheels. Part 2 – fracture wear, J. Eng. Ind., Trans. ASME (1971) 1129–1133.
[11] R.L. Hecker, I.M. Ramoneda, S.Y. Liang, Analysis of wheel topography and grit force for grinding process modeling, J. Manuf. Process. 5 (1) (2003) 13–23.
[12] E. Salje, H. Teiwes, H. Heidenfelder, Important results on external cylindrical plunge grinding with unusual workpiece peripheral speeds and speed ratios q in the range of -0.2 to $-20\,000$, CIRP Ann. – Manuf. Technol. 32 (1) (1983) 241–246.
[13] Z. Zhou, C. Van Lutterwelt, The real contact length between grinding wheel and workpiece – a new concept and a new measuring method, CIRP Ann. – Manuf. Technol. 41 (1) (1992) 387–391.
[14] R. Brown, K. Saito, M. Shaw, Local elastic deflections in grinding, Ann. CIRP 19 (1) (1971) 105–113.
[15] W. Sauer, M. Shaw, The role of elastic deflections of the wheel–work interface in surface grinding, in: Proceedings of the International Conference on Production Engineering, 1974, pp. 645–649.
[16] L. Zhang, T. Suto, H. Noguchi, T. Waida, Applied mechanics in grinding – III. A new formula for contact length prediction and a comparison of available models, Int. J. Mach. Tools Manuf. 33 (4) (1993) 587–597.
[17] W. Rowe, M. Morgan, H. Qi, H. Zheng, The effect of deformation on the contact area in grinding, CIRP Ann. – Manuf. Technol. 42 (1) (1993) 409–412.
[18] J.H. Horng, C.C. Wei, Y.Y. Chen, Y.P. Chang, The microcontact analysis of contact length between wheel and workpiece in precise grinding, in: Advanced Materials Research, vol. 146, Trans Tech Publ, 2011, pp. 1930–1936.
[19] R.P. Lindsay, On the metal removal and wheel removal parameters, surface finish, geometry and thermal damage in precision grinding (Ph.D. thesis), Worcester Polytechnic Institute 1971.
[20] S. Malkin, Grinding Technology, Industrial Press, New York, USA, 2008.
[21] D. André, I. Iordanoff, J.-l. Charles, J. Néauport, Discrete element method to simulate continuous material by using the cohesive beam model, Comput. Methods Appl. Mech. Eng. 213 (2012) 113–125.
[22] D. Andre, J.-L. Charles, I. Iordanoff, 3D Discrete Element Workbench for Highly Dynamic Thermo-mechanical Analysis: GranOO, John Wiley & Sons, London, UK, 2015.
[23] J. Verkerk, Final report concerning CIRP cooperative work on the characterization of grinding wheel topography, Ann. CIRP 26 (2) (1977) 385–395.
[24] N. Brenner, A. Torrance, Wheel sharpness measurement for force prediction in grinding, Wear 160 (2) (1993) 317–323.
[25] G.R. Johnson, W.H. Cook, A constitutive model and data for metals subjected to large strains, high strain rates and high temperatures, in: Proceedings of the 7th International Symposium on Ballistics, vol. 21, The Hague, The Netherlands, 1983, pp. 541–547.
[26] D. Gu, J. Wager, New evidence on the contact zone in grinding contact length, sliding and cutting regions, CIRP Ann. – Manuf. Technol. 37 (1) (1988) 335–338.
[27] Y. Ohbuchi, T. Obikawa, Adiabatic shear in chip formation with negative rake angle, Int. J. Mech. Sci. 47 (9) (2005) 1377–1392.